Adaptive Ensemble-Based Electrochemical-Thermal Degradation State Estimation of Lithium-Ion Batteries

N.B. When citing this work, cite the original published paper.

(article starts on next page)

Adaptive Ensemble-Based Electrochemical-Thermal-Degradation State Estimation of Lithium-Ion Batteries

Yang Li, *Member, IEEE*, Zhongbao Wei, *Senior Member, IEEE*, Binyu Xiong, *Member, IEEE*
and D. Mahinda Vilathgamuwa, *Fellow, IEEE*

Abstract—A computationally efficient state estimation method for lithium-ion (Li-ion) batteries is proposed based on a degradation-conscious high-fidelity electrochemical-thermal model for advanced battery management systems. The computational burden caused by the high-dimensional nonlinear nature of the battery model is effectively eased by adopting an ensemble-based state estimator using the singular evolutive interpolated Kalman filter (SEIKF). Unlike the existing schemes, it shows that the proposed algorithm intrinsically ensures mass conservation without imposing additional constraints, leading to a battery state estimator simple to tune and fast to converge. The model uncertainty caused by battery degradation and the measurement errors are properly addressed by the proposed scheme as it adaptively adjusts the error covariance matrices of the SEIKF. The performance of the proposed adaptive ensemble-based Li-ion battery state estimator is examined by comparing it with some well-established nonlinear estimation techniques that have been used previously for battery electrochemical state estimation, and the results show that excellent performance can be provided in terms of accuracy, computational speed, as well as robustness.

Index Terms—Adaptive estimation, electrochemical state estimation, lithium-ion (Li-ion) battery, singular evolutive interpolated Kalman filter.

NOMENCLATURE

Symbol:

A	Electrode plate area (m^2).
C_T	Battery thermal capacitance (J/K).
D_s	Solid-phase diffusivity (m^2/s).
F	$= 96,485$ C/mol. Faraday constant.
L	Thickness of a domain.
I_{app}	Applied charging current (A).
I_n	Current due to the total molar flux (A).

M	Order of the submodel for solid-phase diffusion.
N^j	Number of control volumes. $j \in \{\text{pos}, \text{sep}, \text{neg}\}$.
N^{tot}	Total number of control volumes.
Q_T	Heat generation (W).
R_T	Battery thermal resistance (K/W).
R_g	$= 8.3145$ J/(mol·K). Universal gas constant.
R_p	Radius of solid particle (m).
R_{ct}	Charge-transfer resistance (Ω).
R_{SEI}	Solid-electrolyte interphase film resistance (Ω).
SOC	State of charge.
SOH	State of health.
T, T_{amb}	Battery and ambient temperatures (K).
U_e	Electrolyte diffusion overpotential (V).
$U_{\text{sr}}^{\text{ref}}$	Reference voltage of the side reactions (V).
U_{ss}	Equilibrium potential of an electrode (V).
V_{bat}	Battery terminal voltage (V).
c_e	Electrolyte concentration (mol/m^3).
c_s	Solid-phase average concentration (mol/m^3).
$\tilde{c}_s$	Solid-phase concentration difference (mol/m^3).
c_{ss}	Solid-phase surface concentration (mol/m^3).
$c_{s,\text{max}}$	Solid-phase maximum concentration (mol/m^3).
j_n	Total molar flux [mol/(m^2· s)].
j_{int}	Intercalation molar flux [mol/(m^2· s)].
j_{sr}	Side reaction molar flux [mol/(m^2· s)].
k_{deg}	Degradation coefficient.
k_0	Electrode reaction constant [m$^{2.5}$/(mol$^{0.5}$· s)].
m, n	Ensemble size, system order.
$n_{s,\text{tot}}^{\text{Li}}$	Amount of cyclable lithium [mol/(m^2)].
t_a^0	Transference number.
u	Input variable.
η_{ct}	Charge-transfer (intercalation) overpotential (V).
η_{sr}	Side-reaction potential (V).
$\eta_{\text{SEI},N}$	SEI side-reaction potential at the separator/negative electrode boundary (V).
δ_R	Forgetting factor for measurement covariance.
$\varepsilon_s, \varepsilon_e$	Solid-phase and electrolyte volume fractions.

Vector and Matrix:

$\mathbf{0}, \mathbf{1}, \mathbf{I}$	Zero matrix, unity matrix, identity matrix.
$\mathbf{A}, \mathbf{C}$	Transformation matrix, Matrix square root of $\mathbf{A}$.
$\mathbf{K}_e$	Ensemble Kalman gain.
$\mathbf{P}$	State covariance matrix.
$\mathbf{Q}$	Process noise covariance matrix.
$\mathbf{R}$	Measurement noise covariance matrix.
$\mathbf{T}$	A matrix with full rank and zero column sums.

U, S, V	Singular value decomposition of $\mathbf{A}^{-1}$.
ϵ	Residual vector.
$\mathbf{v}$, $\mathbf{n}$	Process and measurement noise vectors.
$\bar{\mathbf{w}}$, $\tilde{\mathbf{W}}$	Weight vector, weight matrix.
$\mathbf{x}$, $\mathbf{X}$	State vector, state ensemble matrix.
$\bar{\mathbf{x}}$, $\tilde{\mathbf{X}}$	Mean and perturbation matrix of state ensemble.
$\mathbf{y}$	Unmeasurable output vector.
$\mathbf{z}$, $\mathbf{Z}$	Measurement, measurement ensemble matrix.
$\bar{\mathbf{z}}$, $\tilde{\mathbf{Z}}$	Mean and perturbation matrix of measurement ensemble.

Subscript:

i	Control volume index. $i \in \{1, 2, \cdots, N^{\text{tot}}\}$.
k	Discrete time index. $k \in \{0, 1, \cdots\}$.
0	Initial value.
0%, 100%	Value at SOC = 0% or SOC = 100%.

Superscript:

neg, pos	Negative electrode, positive electrode.
sep	Separator.
$+$, $-$	Posterior estimate, prior estimate.
p	Ensemble member index. $p \in \{1, 2, \cdots, m\}$.
q	State variable index. $q \in \{1, 2, \cdots, n\}$.

I. INTRODUCTION

LITHIUM-ION (Li-ion) battery has become the leading electrochemical energy storage technology due to its salient advantages of high power and high energy densities, low self-discharge rate, favorable modularity, and recent rapid decline in cost. It has been widely adopted in modern industrial applications such as in smart grids with a high penetration of renewables and electrified vehicles [1]. The increasing need for higher safety and longer service life of Li-ion battery that is amenable to a wider operating range has lead to some extensive research efforts to develop advanced battery management systems (ABMSs) [2].

In an ABMS, monitoring the health- and safety-related internal states, such as the lithium-ion concentrations, side-reaction potentials, internal temperature, cell strain, gas e-mission, as well as the internal resistance of the battery, is of primary importance to achieve safe, reliable, and efficient operation of the battery systems. Nevertheless, it is difficult to physically measure these internal states in practice based on the prevailing sensor technology. Hence, electrochemical state estimation techniques, that have been developed with the external measurements of terminal voltage, applied current, and surface temperature of the battery, have received growing research attention in recent years. These techniques usually rely on physics-based models which are established based on underlying electrochemical principles. The information on the internal states can be utilized for designing health- and safety-aware battery charging control [3] and energy management [4], in contrast to using conventional empirical battery models such as a lumped-parameter equivalent circuit model (ECM) [5] or data-driven techniques [6] to develop such battery control and management schemes.

Described by partial differential algebraic equations (P-DAEs), the rigorous physics-based model of the Li-ion batteries, namely the pseudo two-dimensional (P2D) model, was originally developed for Li-ion battery design but can hardly be implementable in real-time control systems due to its prohibitively high computational cost [7]. To overcome such a difficulty, extensive research efforts have been made to simplify the distributed-parameter physics-based models. Early research on estimating the battery state of charge (SOC) with nonlinear estimators has been constructed using the single particle model (SPM) and its improved versions, where the influence of the nonuniformity in the electrode is ignored. These include the extended Kalman filter (EKF) with the SPM [8], unscented Kalman filter (UKF) with an enhanced SPM adding the electrolyte dynamics [9], backstepping observer based on an SPM enhanced with electrolyte dynamics [10], moving horizon estimation with the enhanced SPM that captures electrolyte [11] and thermal [12] dynamics, and co-estimation of SOC and state of health (SOH) using particle filter (PF) [13]. However, electrode uniformity assumption is held only under low to medium current rates, and it can be largely violated under today's high-power and high-energy battery charging conditions. In addition, the extended operating range can lead to a significant nonuniform degradation behavior in the electrode [14], which cannot be captured by the above electrochemical state estimators for accurate battery health state monitoring.

To better predict the local performance of an electrode, various electrochemical state estimators are designed with simplified P2D models based on the EKF [15], the UKF [16], and the PF [17], with the incorporation of nonuniformity of the electrode. However, the computational complexities of these state estimators are in the order $\mathcal{O}(n^3)$, where n is the system order [18]. Such battery state estimation techniques are saddled with high computational costs for online operation due to the large n of the electrochemical models with spatially distributed states and parameters. High-performance processors and parallel computing techniques need to be adopted to obtain reasonable computational efficiency [16]. However, this solution is not cost-effective for most real-time systems where the computational resources are primarily selected for low-order ECM-based battery management. In order to substantially reduce the computational burden, an efficient electrochemical battery state estimator is designed based on the ensemble Kalman filter (EnKF) [19], where a physics-based equivalent circuit network reformulated from the P2D model is efficiently solved. In the EnKF, the sequential Monte Carlo method is applied to the conventional Kalman filter. Since the large-size n-by-n covariance matrix approximated with a low-rank (n-by-m) ensemble matrix, the computational burden can thus be significantly lightened [20].

It is worth noting that the computational superiority of the EnKF to conventional algorithms, such as EKF and UKF, only exists under the condition $m \ll n$, leading to a very small m in the battery electrochemical state estimator under investigation. As the statistical characteristics may not be correctly represented with a small set of randomly perturbed samples in the EnKF, the performance of the battery estimator can

be significantly lowered and it may even cause a divergence due to the undersampling issue [21]. In this work, as the first contribution, we address the problem by bridging an ensemble-based square-root state estimation technique and a high-dimensional physics-based model. The problem-causing perturbed measurement is avoided and the capability of the ensemble-based battery state estimator to track the battery SOH is demonstrated for the first time with the incorporated battery degradation phenomena.

Although it is well-recognized that the performance of most nonlinear state estimation algorithms significantly depends on the method of choosing the estimator parameters, in the existing works it is rarely discussed in relation to physics-model-based battery state estimation. As most systematic and empirical parameter tuning methods in the literature are usually application-dependent with certain assumptions on the system model, e.g., EKF and UKF, their applicability to the present problem for battery state estimation is unknown. In this regard, the proposed ensemble-based battery state estimator offers a robust and fast initialization process that only needs a simple parameter tuning procedure. In addition, we prove that mass conservation is intrinsically guaranteed in the proposed ensemble-based battery state estimator. Hence, the additional steps to impose constraints on mass conservation are avoided. These steps are necessary for enhancing the estimator convergence in the existing works. This leads to simpler implementation and reduced computational burden.

Furthermore, the information of uncertainties is assumed known in the previous work [19], possibly being identified offline and obtained from sensor specification. However, in practice, the error covariances can be changed due to various factors such as battery aging and faults of the measurement devices. The use of constant covariance matrices during the lifetime of the battery can result in substantial estimation errors and even filtering divergence. Recent studies have investigated adaptive filtering schemes for battery electrochemical state estimator based on EKF [22] and UKF [22], [23] suitable for low-order systems. A proposed ensemble-based method to efficiently incorporate adaptiveness into the battery estimator with high-dimensional physics-based model forms another contribution of the present investigation.

II. ELECTROCHEMICAL-THERMAL-DEGRADATION MODEL OF LI-ION BATTERY

A. P2D Model With Thermal Dynamics

The P2D model of Li-ion batteries was established based on the porous electrode theory and the concentrated solution theory [7]. It is a general modeling framework for a Li-ion cell with the sandwich-like structure with three domains, namely the positive electrode (i.e., the cathode, denoted by "pos"), the negative electrode (i.e., the anode, denoted by "neg"), and the separator (denoted by "sep"). The lithium ions are stored in a number of assumed spherical particles in the solid phase of the electrode, and the transport of the lithium ions during charge/discharge would cause the variation of the concentrations in the particles as well as in the electrolyte. A set of tightly coupled and highly nonlinear PDAEs are used to
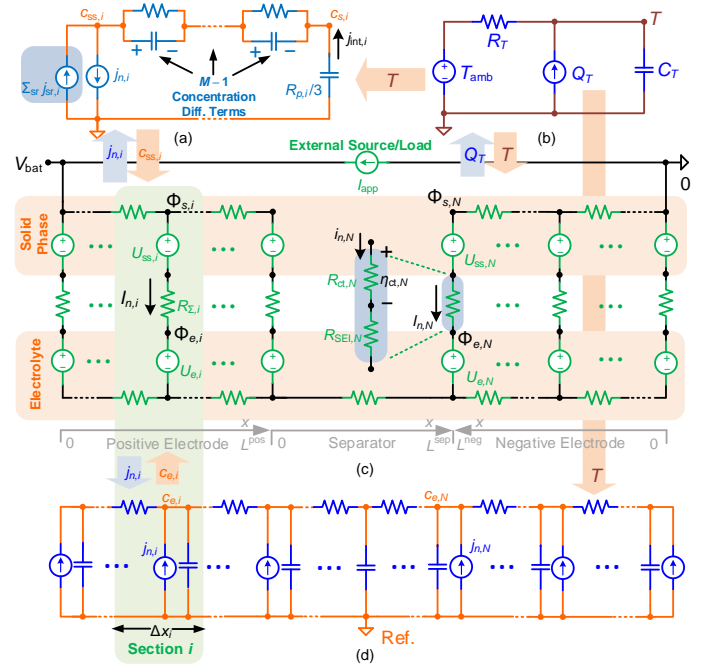

Fig. 1. Equivalent circuit representation of physics-based model of a Li-ion battery cell, including the subcircuits that describe (a) mass transport in a solid particle, (b) heat transfer, (c) charge transport in the electrolyte, and (d) mass transport in the electrolyte.

describe the cell behaviors in the horizontal axis (x-direction) on the macro scale as well as the pseudo radial axis on the micro scale. A thermal model can be readily incorporated into the P2D framework to form a coupled electrochemical-thermal model, denoted by the *P2D-T model* in this work.

B. A Reduced-Order Electrochemical-Thermal Model

A transmission-line-like equivalent circuit as depicted in Fig. 1 can be used to illustrate the structure of the P2D-T model. The subcircuit in Fig. 1(c) was obtained by applying the finite volume method along the x-direction. The domains of the positive electrode, separator, and negative electrode are divided into N^{pos}, N^{sep}, and N^{neg} control volumes, respectively. The subscript $i \in \{1, 2, \cdots, N^{tot}\}$ indicates the local quantities at the ith control volume, where $N^{tot} = N^{pos} + N^{sep} + N^{neg}$ is the total number of control volumes. This reduced-order model (ROM) will be briefly explained next and the physical meanings of the symbols are provided in the Nomenclature.

In Fig. 1(c), V_{bat} is the terminal voltage and I_{app} is the applied current. In each section i, the diffusion of the lithium species in the solid phase is modeled by an Mth-order equivalent circuit shown in Fig. 1(a), where $c_{s,i}$ and $c_{ss,i}$ represent the volumed-averaged and the surface concentrations, respectively. The battery SOC can be calculated using all $c_{s,i}$ in the negative electrode, i.e.,

$$\text{SOC}(t) = \frac{\frac{1}{N^{neg}} \sum_{i=N^{pos}+N^{sep}+1}^{N^{tot}} c_{s,i}(t) - c_{s,0\%}^{neg}}{c_{s,100\%}^{neg} - c_{s,0\%}^{neg}} \quad (1)$$

The voltage sources $U_{ss,i}$ and $U_{e,i}$ in Fig. 1(c) are concentration-dependent nonlinear functions: the open-

circuit potential (OCP) $U_{ss,i} = f_{OCP}^i(c_{ss,i})$ is determined by the active material of the electrode, and $U_{e,i} = (2R_g T t_a^0/F)\ln(c_{e,i}/c_{e0})$ is associated with the electrolyte concentration $c_{e,i}$ governed by the diffusion subcircuit in Fig. 1(d). The battery temperature T is described by a lumped heat transfer model as shown in Fig. 1(b), where the generated heat Q_T is calculated as the total power losses generated from the equivalent circuit in Fig. 1(c) and T also affects the parametric values of the circuit elements in Figs. 1(a), (b) and (d). In addition, the molar flux source $j_{n,i}$ in Fig. 1(a) and Fig. 1(d) is proportional to the branch current $I_{n,i}$ in Fig. 1(c). The readers are referred to previous works such as [19], [24] for detailed information on this coupled electrochemical-thermal ROM.

C. Model Extension With Degradation

The battery model presented in Section II-B describes the intercalation/de-intercalation processes of a Li-ion battery cell during charging and discharging. Since the performance of Li-ion batteries can degrade gradually over time, an extension of the model is required for monitoring aging-related behaviors and designing battery health management strategies.

In this work, the loss of lithium inventory (LLI) due to side reactions, as a consequence of solid-electrolyte interphase (SEI) film growth and lithium plating (LiP) in the negative electrode, is considered the major degradation mode that affects the battery SOH [25]. The SOH is thus associated with the amount of total cyclable lithium $n_{s,tot}^{Li}$ in the solid phase of the electrodes, calculated by

$$n_{s,tot}^{Li}(t) = \frac{\varepsilon_s^{pos} L^{pos}}{N^{pos}} \sum_{i=1}^{N^{pos}} c_{s,i}(t) + \frac{\varepsilon_s^{neg} L^{neg}}{N^{neg}} \sum_{\substack{i=N^{pos}+\\N^{sep}+1}}^{N^{tot}} c_{s,i}(t) \quad (2)$$

$$\text{SOH}(t) = \frac{n_{s,tot}^{Li}(t)}{n_{s,tot0}^{Li}} \quad (3)$$

where $n_{s,tot0}^{Li}$ is the amount of the cyclable lithium at the beginning of life (BOL) of the battery cell.

To incorporate the degradation behaviors, in Fig. 1(a), the total molar flux $j_{n,i}$ is considered as the sum of the intercalation molar flux $j_{int,i}$ and all side reaction molar fluxes $\Sigma_{sr} j_{sr,i}$. Each side reaction molar flux $j_{sr,i}$ has a complex nonlinear functional relationship $\phi_{sr,i}(\cdot)$ with the local variables (See. e.g. [14], [26], [27]), generally expressed as

$$j_{sr,i}(t) = \phi_{sr,i}(\eta_{sr,i}(t), T(t), c_{ss,i}(t), c_{e,i}(t), \cdots) \quad (4)$$

$$\eta_{sr,i}(t) = U_{ss,i}(t) + R_{ct,i} I_{n,i}(t) - U_{sr}^{ref} \quad (5)$$

$\forall i \in \{N^{pos} + N^{sep} + 1, \cdots N^{tot}\}$, $\forall sr \in \{\text{SEI}, \text{LiP}, \cdots\}$, where $\eta_{sr,i}$ is the side reaction potential (SRP), U_{sr}^{ref} is side reaction reference voltage, $R_{ct,i} = R_g T/[F^2 k_{0,i} A c_{e,i}^{0.5} c_{ss,i}^{0.5}(c_{s,max,i} - c_{ss,i})^{0.5}]$ is the charge-transfer resistance as shown in Fig. 1(c). The SRP $\eta_{sr,i}$ at the separator/negative electrode boundary is an important variable to monitor as its magnitude affects the side reaction rate. Note that the sum of all local side reactions $\Sigma_{sr} j_{sr,i}$ is always negative. According to Fig. 1(a), the condition $\Sigma_{sr} j_{sr,i}(t) < 0, \forall t > 0$ causes continuous reductions in the solid-phase concentration $c_{s,i}$, and thus both $n_{s,tot}^{Li}$ and

SOH will gradually decrease over time according to (2) and (3) as the result of LLI.

However, it is difficult to accurately describe all the side reactions with $\phi_{sr,i}(\cdot)$ and efficiently solve the complex aging model coupled with the circuit model presented in Fig. 1. A simple degradation model is thus adopted based on the fact that side-reaction-induced degradation has ignorable effects on battery performance during a short period of time (e.g. in one hour). Usually, the magnitude of $j_{sr,i}$ is much smaller than that of $j_{n,i}$, and the resulting LLI is thus small. It will be sufficiently reasonable to assume that

$$\Sigma_{sr} j_{sr,i}(t) = -k_{deg} \quad (6)$$

$\forall i \in \{N^{pos} + N^{sep} + 1, \cdots N^{tot}\}$, where $0 < k_{deg} \ll 1$ is a small positive coefficient explained as the average of the side reaction rates across the electrode. k_{deg} will be estimated as a slowly-varying state in this work.

D. Model Summary

After being discretized in the time domain with the time step of Δt, the ROM extended with degradation can be expressed in a discrete-time state-space form [19],

$$\mathbf{x}_k = \mathcal{F}(\mathbf{x}_{k-1}, u_k, \Delta t) + \mathbf{v}_k \quad (7a)$$

$$\mathbf{z}_k = \mathcal{H}(\mathbf{x}_k, u_k) + \mathbf{n}_k \quad (7b)$$

$$\mathbf{y}_k = \mathcal{L}(\mathbf{x}_k, u_k) \quad (7c)$$

where the subscript $k = t/\Delta t$ is the discrete time index. $\mathcal{F}(\cdot)$, $\mathcal{H}(\cdot)$, and $\mathcal{L}(\cdot)$ are nonlinear operators for the process, measurable, and unmeasurable output, respectively. The state vector $\mathbf{x} = [(\mathbf{c}_s^{pos})^\top, (\mathbf{c}_s^{neg})^\top, (\mathbf{c}_e)^\top, (\tilde{\mathbf{c}}_s)^\top, T, k_{deg}]^\top \in \mathbb{R}^n$ consists of all the local concentrations and battery temperature augmented with the degradation coefficient k_{deg}, and the system order is $n = M(N^{pos} + N^{neg}) + N^{tot} + 2$. Here, $\mathbf{c}_s^{pos} \in \mathbb{R}^{N^{pos}}$ and $\mathbf{c}_s^{neg} \in \mathbb{R}^{N^{neg}}$ consist of the local volume-averaged concentrations $c_{s,i}$ in the positive and the negative electrodes, respectively, $\mathbf{c}_e \in \mathbb{R}^{N^{tot}}$ consists of the local electrolyte concentrations $c_{e,i}$ in Fig. 1(d), and $\tilde{\mathbf{c}}_s \in \mathbb{R}^{(M-1)(N^{pos}+N^{neg})}$ contains the local concentration difference terms as indicated in Fig. 1(a). The model input is the current $u = I_{app}$, and the measurements include the battery voltage and ambient temperature, i.e., $\mathbf{z} = [V_{bat}, T_{amb}]^\top$. The uncertainties of the process and the measurements are also considered in (7) by introducing the normally distributed error vectors $\mathbf{v} \sim \mathcal{N}(\mathbf{0}, \mathbf{Q})$ and $\mathbf{n} \sim \mathcal{N}(\mathbf{0}, \mathbf{R})$, respectively. Furthermore, the unmeasurable output vector $\mathbf{y}$ includes SOC, SOH, SRPs, etc. These variables are of interest for health-aware battery management diagnosis and control, and all of them can be explicitly expressed as functions of the state vectors and the input current by solving the circuit model.

III. ADAPTIVE STATE ESTIMATION USING SINGULAR EVOLUTIVE INTERPOLATED KALMAN FILTER

In this section, an ensemble-based electrochemical state estimator is designed to observe the high-dimensional internal states of the Li-ion batteries using the ROM summarized in Section II-D. The proposed battery state estimator is based

on the singular evolutive interpolated Kalman filter (SEIKF), a square-root type filtering algorithm originally introduced by Pham *et al.* for oceanographical studies [28], [29]. We reformulate the SEIKF based on the algorithm described in [30], with notations being modified to provide better readability for the battery management community. In an ensemble-based method, an n-by-m state ensemble matrix is used to approximate the n-by-n covariance matrix, defined as

$$\hat{\mathbf{X}}_k := [\hat{\mathbf{x}}_k^{(1)}, \hat{\mathbf{x}}_k^{(2)}, \cdots, \hat{\mathbf{x}}_k^{(m)}] \in \mathbb{R}^{n \times m}.$$

Each column of the state ensemble matrix, called an *ensemble member*, is a sample estimate of the n-dimensional state vector defined in Section II-D. The *ensemble mean* $\bar{\mathbf{x}}_k$ and *ensemble perturbation matrix* $\tilde{\mathbf{X}}_k$ are defined as follows.

$$\bar{\mathbf{x}}_k := \frac{1}{m} \sum_{p=1}^{m} \hat{\mathbf{x}}_k^{(p)} \tag{8a}$$

$$\tilde{\mathbf{X}}_k := \hat{\mathbf{X}}_k - \overbrace{[\bar{\mathbf{x}}_k, \bar{\mathbf{x}}_k, \cdots, \bar{\mathbf{x}}_k]}^{m}. \tag{8b}$$

A. Initialization

The battery state estimator is first initialized by choosing a proper initial state ensemble $\hat{\mathbf{X}}_0^+ := [\hat{\mathbf{x}}_0^{+(1)}, \hat{\mathbf{x}}_0^{+(2)}, ..., \hat{\mathbf{x}}_0^{+(m)}]$. The element in the qth row and the pth column in $\hat{\mathbf{X}}_0^+$ is

$$\hat{\mathbf{X}}_0^{+(q,p)} = \begin{cases} c_{s0}^{\text{pos}(p)}, & \forall q \in \mathcal{S}_s^{\text{pos}} \\ c_{s0}^{\text{neg}(p)}, & \forall q \in \mathcal{S}_s^{\text{neg}} \\ c_{e0}, & \forall q \in \mathcal{S}_e \\ T_0, & q = n-1 \\ k_{\text{deg}0}, & q = n \\ 0 & \text{otherwise} \end{cases} \tag{9}$$

where $\mathcal{S}_s^{\text{pos}} := \{1, 2, \cdots, N^{\text{pos}}\}$, $\mathcal{S}_s^{\text{neg}} := \{N^{\text{pos}} + 1, \cdots N^{\text{pos}} + N^{\text{neg}}\}$, and $\mathcal{S}_e := \{N^{\text{pos}} + N^{\text{neg}} + 1, \cdots, N^{\text{pos}} + N^{\text{neg}} + N^{\text{tot}}\}$ are the index sets for the elements in $\mathbf{c}_s^{\text{pos}}$, $\mathbf{c}_s^{\text{neg}}$, and $\mathbf{c}_e$, respectively. It assumes that the solid-phase concentration states in $\hat{\mathbf{X}}_0^+$ uniformly covers an estimated range of SOC from $\text{SOC}_0^{\text{min}}$ to $\text{SOC}_0^{\text{max}}$ as shown in Fig. 2, i.e.,

$$\text{SOC}_0^{(p)} = \text{SOC}_0^{\text{min}} + (p/m)(\text{SOC}_0^{\text{max}} - \text{SOC}_0^{\text{min}}) \tag{10a}$$

$$c_{s0}^{\text{pos}(p)} = (c_{s,0\%}^{\text{pos}} - c_{s,100\%}^{\text{pos}})\text{SOC}_0^{(p)} + c_{s,100\%}^{\text{pos}} \tag{10b}$$

$$c_{s0}^{\text{neg}(p)} = (c_{s,100\%}^{\text{neg}} - c_{s,0\%}^{\text{neg}})\text{SOC}_0^{(p)} + c_{s,0\%}^{\text{neg}} \tag{10c}$$

$\forall p \in \{1, 2, \cdots, m\}$. In addition, the initial electrolyte concentration c_{e0} is a known battery parameter determined by the electrolyte characteristics, the initial battery temperature T_0 is measurable using a temperature sensor, and the initial degradation coefficient $k_{\text{deg}0}$ can be set as follows. Within a time period $\Delta\tau$, according to Fig. 1(a), the change in the solid-phase concentration $\Delta c_{s,i}$ caused by $\Sigma_{\text{sr}} j_{\text{sr},i}$ is obtained by

$$\Delta c_{s,i} = \frac{3}{R_p^i}(\Sigma_{\text{sr}} j_{\text{sr},i})\Delta\tau = -\frac{3}{R_p^{\text{neg}}} k_{\text{deg}0}\Delta\tau \tag{10d}$$

According to (2) and (3), this reduction in concentration leads to the decrease of $n_{s,\text{tot}}^{\text{Li}}$ and SOH, i.e.,

$$\Delta\text{SOH} = \frac{\Delta n_{s,\text{tot}}^{\text{Li}}}{n_{s,\text{tot}0}^{\text{Li}}} = \frac{\varepsilon_s^{\text{neg}} L^{\text{neg}}}{n_{s,\text{tot}0}^{\text{Li}}} \Delta c_{s,i} \tag{10e}$$
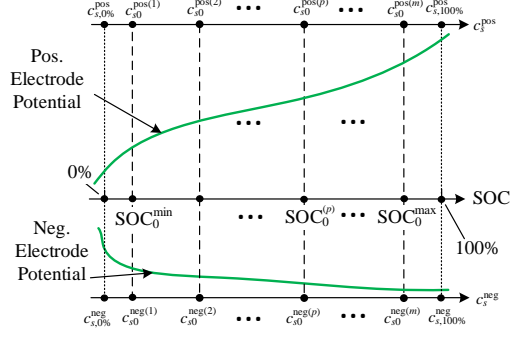

Fig. 2. Initial setting of solid-phase concentrations in state ensemble.

With (10d) and (10e), $k_{\text{deg}0}$ can be calculated according to the rate of change of the SOH ($\Delta\text{SOH}/\Delta\tau$)

$$k_{\text{deg}0} = \frac{\Delta\text{SOH}}{\Delta\tau} \frac{n_{s,\text{tot}0}^{\text{Li}}}{\varepsilon_s^{\text{neg}} L^{\text{neg}}} \frac{R_p^{\text{neg}}}{3} \tag{10f}$$

B. Prediction Step

Based on the previous-step $((k-1)$th) posterior state ensemble matrix $\hat{\mathbf{X}}_{k-1}^+ := [\hat{\mathbf{x}}_{k-1}^{+(1)}, \hat{\mathbf{x}}_{k-1}^{+(2)}, ..., \hat{\mathbf{x}}_{k-1}^{+(m)}]$, the current-step ($k$th) prior state ensemble matrix $\hat{\mathbf{X}}_k^- := [\hat{\mathbf{x}}_k^{-(1)}, \hat{\mathbf{x}}_k^{-(2)}, ..., \hat{\mathbf{x}}_k^{-(m)}]$ is predicted by forwarding each ensemble member according to the state equation (7a). Thus,

$$\hat{\mathbf{x}}_k^{-(p)} = \mathcal{F}(\hat{\mathbf{x}}_{k-1}^{+(p)}, u_k, \Delta t) + \hat{\mathbf{v}}_k^{(p)} \quad \forall p \in \{1, 2, \cdots, m\} \tag{11}$$

where the process noise $\hat{\mathbf{v}}_k^{(p)}$ is drawn from normal distribution $\mathcal{N}(0, \hat{\mathbf{Q}}_k)$ i.i.d..

C. Update Step

The purpose of the update step of an ensemble-based filter is to assimilate the latest measurements $\mathbf{z}_k$ to obtain the posterior state ensemble $\hat{\mathbf{X}}_k^+ := [\hat{\mathbf{x}}_k^{+(1)}, \hat{\mathbf{x}}_k^{+(2)}, ..., \hat{\mathbf{x}}_k^{+(m)}]$. For both EnKF and SEIKF, a measurement ensemble $\hat{\mathbf{Z}}_k := [\hat{\mathbf{z}}_k^{(1)}, \hat{\mathbf{z}}_k^{(2)}, ..., \hat{\mathbf{z}}_k^{(m)}]$ is generated. Each member of $\hat{\mathbf{Z}}_k$ is obtained according to (7b), i.e.,

$$\hat{\mathbf{z}}_k^{(p)} = \mathcal{H}(\hat{\mathbf{x}}_k^{-(p)}, u_k) \quad \forall p \in \{1, 2, \cdots, m\} \tag{12a}$$

Similar to (8), the ensemble mean and ensemble perturbation matrix of $\hat{\mathbf{Z}}_k$ can be defined by

$$\bar{\mathbf{z}}_k = \frac{1}{m} \sum_{p=1}^{m} \hat{\mathbf{z}}_k^{(p)} \tag{12b}$$

$$\tilde{\mathbf{Z}}_k = \hat{\mathbf{Z}}_k - \overbrace{[\bar{\mathbf{z}}_k, \bar{\mathbf{z}}_k, \cdots, \bar{\mathbf{z}}_k]}^{m}. \tag{12c}$$

In the EnKF, the member of the posterior state ensemble $\hat{\mathbf{X}}_k^+$ is obtained by

$$\mathbf{K}_{e,k} = \frac{\tilde{\mathbf{X}}_k^- \tilde{\mathbf{Z}}_k^\top}{m-1} \left(\frac{\tilde{\mathbf{Z}}_k \tilde{\mathbf{Z}}_k^\top}{m-1} + \hat{\mathbf{R}}_k\right)^{-1} \tag{13a}$$

$$\hat{\mathbf{x}}_k^{+(p)} = \hat{\mathbf{x}}_k^{-(p)} + \mathbf{K}_{e,k}(\mathbf{z}_k + \mathbf{n}_k^{(p)} - \hat{\mathbf{z}}_k^{(p)}) \tag{13b}$$

5

$\forall p \in \{1, 2, \cdots, m\}$. Here, $\mathbf{K}_{e,k}$ is ensemble Kalman gain, and $\mathbf{n}_k^{(p)} \sim \mathcal{N}(\mathbf{0}, \hat{\mathbf{R}}_k)$ is the pseudo measurement perturbation intentionally added to obtain the correct error covariance. The ensemble mean $\bar{\mathbf{x}}_k^+$, calculated from $\hat{\mathbf{X}}_k^+$, is considered the estimate of the system state and used to calculate the output vector according to (7c).

The ensemble size m should be large enough to correctly represent the error characteristics when the pseudo measurement perturbation is randomly generated in the update step in the EnKF. In contrast, perturbed measurements are not used in the SEIKF. Instead, $\hat{\mathbf{X}}_k^+$ is calculated by updating the ensemble mean $\bar{\mathbf{x}}_k^+$ and the ensemble perturbation matrix $\tilde{\mathbf{X}}_k^+$ separately, and both are considered linear transformations of the prior counterparts, i.e.,

$$\bar{\mathbf{x}}_k^+ = \bar{\mathbf{x}}_k^- + \tilde{\mathbf{X}}_k^- \bar{\mathbf{w}}_k \quad \text{(14a)}$$

$$\tilde{\mathbf{X}}_k^+ = \tilde{\mathbf{X}}_k^- \tilde{\mathbf{W}}_k \quad \text{(14b)}$$

where the weight vector $\bar{\mathbf{w}}_k$ and the weight matrix $\tilde{\mathbf{W}}_k$ are calculated according to

$$\bar{\mathbf{w}}_k = \mathbf{T}\mathbf{A}_k (\hat{\mathbf{Z}}_k \mathbf{T})^\top \hat{\mathbf{R}}_k^{-1}(\mathbf{z}_k - \bar{\mathbf{z}}_k) \quad \text{(14c)}$$

$$\tilde{\mathbf{W}}_k = \sqrt{m-1}\mathbf{T}\mathbf{C}_k \boldsymbol{\Omega}_k^\top. \quad \text{(14d)}$$

and $\mathbf{T} \in \mathbb{R}^{m \times (m-1)}$ is a static matrix with full rank and zero column sums, given by

$$\mathbf{T} = \begin{bmatrix} \mathbf{I}_{m-1} \\ \mathbf{0}_{1 \times (m-1)} \end{bmatrix} - \frac{1}{m}\left[\mathbf{1}_{m \times (m-1)}\right] \quad \text{(14e)}$$

where $\mathbf{I}$, $\mathbf{0}$, and $\mathbf{1}$ represent the identity matrix, zero matrix, and unity matrix, respectively, with the subscripts being the matrix dimensions. Multiplying an ensemble matrix by $\mathbf{T}$ simply calculates the corresponding ensemble perturbation matrix and then removes its last column.

In (14c) and (14d), $\mathbf{A}_k \in \mathbb{R}^{(m-1) \times (m-1)}$ is a transformation matrix and $\mathbf{C}_k$ is a matrix square root of $\mathbf{A}_k$, obtained by

$$\mathbf{A}_k = \left[(m-1)\mathbf{T}^\top \mathbf{T} + (\hat{\mathbf{Z}}_k \mathbf{T})^\top \hat{\mathbf{R}}_k^{-1}(\hat{\mathbf{Z}}_k \mathbf{T})\right]^{-1} \quad \text{(14f)}$$

$$\mathbf{A}_k^{-1} = \mathbf{U}_k \mathbf{S}_k \mathbf{V}_k^{-1} \quad \text{(14g)}$$

$$\mathbf{C}_k = \mathbf{U}_k (\mathbf{S}_k)^{-\frac{1}{2}} \mathbf{U}_k^\top. \quad \text{(14h)}$$

where (14g) is the singular value decomposition of $\mathbf{A}_k^{-1}$.

Furthermore, in (14d), $\boldsymbol{\Omega}_k \in \mathbb{R}^{m \times (m-1)}$ is a matrix with its columns being orthonormal and orthogonal to unity vector. A method to obtain $\boldsymbol{\Omega}_k$ is presented in Appendix A.

D. Adaptive Adjustment of Covariance Matrices

The covariance matrices $\mathbf{R}_k$ and $\mathbf{Q}_k$ are usually known exactly and they are affected due to degradation and faults of both the battery and its measurements. A method to online adjust the covariance matrices in the SEIKF-based battery state estimator is proposed in this subsection.

First, the measurement error covariance matrix $\mathbf{R}_k$ can be estimated using measurement residual [31]. A general definition is used here [32], i.e.,

$$\mathbf{R}_k = \mathbb{E}\left[\mathbf{n}_k \mathbf{n}_k^\top\right] = \mathbb{E}\left[\boldsymbol{\epsilon}_k \boldsymbol{\epsilon}_k^\top\right] + \mathbf{P}_{zz,k}^+ \quad \text{(15)}$$

where $\mathbb{E}[\cdot]$ represents the expected value, $\boldsymbol{\epsilon}_k$ is the residual and $\mathbf{P}_{zz,k}^+$ is the residual covariance. To approximate the expected value, a small forgetting factor $0 < \delta_R \ll 1$ is used here to prevent short-term fluctuation in the estimated results, i.e.,

$$\hat{\mathbf{R}}_{k+1} = (1 - \delta_R)\hat{\mathbf{R}}_k + \delta_R\left(\boldsymbol{\epsilon}_k \boldsymbol{\epsilon}_k^\top + \mathbf{P}_{zz,k}^+\right). \quad \text{(16)}$$

In the SEIKF, the residual and the residual covariance can be readily approximated using ensemble $\hat{\mathbf{Z}}_k^+ := [\hat{\mathbf{z}}_k^{+(1)}, \hat{\mathbf{z}}_k^{+(2)}, ..., \hat{\mathbf{z}}_k^{+(m)}]$, i.e.,

$$\hat{\mathbf{z}}_k^{+(p)} = \mathcal{H}(\hat{\mathbf{x}}_k^{+(p)}, u_k) \quad \forall p \in \{1, 2, \cdots, m\} \quad \text{(17a)}$$

$$\boldsymbol{\epsilon}_k = \mathbf{z}_k - \bar{\mathbf{z}}_k^+ \quad \text{(17b)}$$

$$\mathbf{P}_{zz,k}^+ = \frac{1}{m-1}\left(\tilde{\mathbf{Z}}_k^+\right)^\top \tilde{\mathbf{Z}}_k^+. \quad \text{(17c)}$$

where $\bar{\mathbf{z}}_k^+$ and $\tilde{\mathbf{Z}}_k^+$ are the mean vector and perturbation matrix of $\hat{\mathbf{Z}}_k^+$, respectively.

On the other hand, the model error covariance matrix $\mathbf{Q}_k$ is defined by

$$\mathbf{Q}_k = \mathbb{E}\left[\mathbf{v}_k \mathbf{v}_k^\top\right]. \quad \text{(18)}$$

According to (7a) and (14a), the process noise can be estimated by

$$\hat{\mathbf{v}}_k = \bar{\mathbf{x}}_k^+ - \mathcal{F}(\bar{\mathbf{x}}_{k-1}^+, u_k, \Delta t) = \bar{\mathbf{x}}_k^+ - \bar{\mathbf{x}}_k^- = \tilde{\mathbf{X}}_k^- \bar{\mathbf{w}}_k. \quad \text{(19)}$$

To obtain the expected value in (18), a similar procedure can be adopted to smooth $\hat{\mathbf{Q}}_k$ using a forgetting factor. However, it demands additional computational resource to process $\hat{\mathbf{Q}}_k$ with dimension n-by-n, for use in the next time-step. As will be shown in the latter sections, the fluctuation in $\hat{\mathbf{Q}}_k$ has ignorable effects on the short-term performance of the SEIKF. Hence, the need for smoothing $\hat{\mathbf{Q}}_k$ can be avoided by the approximation:

$$\hat{\mathbf{Q}}_{k+1} = \left(\tilde{\mathbf{X}}_k^- \bar{\mathbf{w}}_k\right)\left(\tilde{\mathbf{X}}_k^- \bar{\mathbf{w}}_k\right)^\top. \quad \text{(20)}$$

IV. DISCUSSION ON ADAPTIVE ENSEMBLE-BASED BATTERY STATE ESTIMATOR

A. Computational Requirement

In the SEIKF, only an n-by-m ensemble matrix $\hat{\mathbf{X}}_k^+$ needs to be maintained and evolved. The leading cost in the SEIKF is in the order of $\mathcal{O}(nm + nm^2)$ to perform (14a) and (14b) when $m \ll n$. On the contrary, for EKF- and UKF-based algorithms, both the mean $\bar{\mathbf{x}}_k^+$ of the state estimate and the n-by-n covariance matrix $\hat{\mathbf{P}}_k^+$ need to be dealt with, and their leading costs are in the order of $\mathcal{O}(n^3)$ [18]. Also, the SEIKF is advantageous over EKF as there is no need to perform sequential linearization, in which calculating a set of large-size Jacobian matrices online can be extremely heavy for the highly nonlinear coupled battery model. Hence, the SEIKF algorithm is much more computationally efficient to implement than the widely adopted stochastic nonlinear filtering algorithms such as EKF and UKF.

The behavior of the SEIKF and EnKF for nonlinear models is examined and compared in [29], where it is found that the SEIKF can be more efficient than the EnKF because a smaller ensemble could be used to achieve comparable estimation errors [33]. Although more equations are used in the update

step of the SEIKF compared to the EnKF, as can be seen from Section III-C, since the dimensions of the matrices such as $\mathbf{A}_k$, $\mathbf{C}_k$, $\mathbf{T}$, and $\mathbf{\Omega}_k$ are low, the additional computational requirement to execute (14c)–(14h) overhead is small.

B. Parameter Tuning

The ensemble size m is the only parameter to be determined for the SEIKF- and the EnKF-based estimators. Starting from $m = 2$, different tests can be carried out by increasing m until the filters converge fast and the RMSE of the estimated SOC is less than, e.g., 1%. Also, the initial guess of the SOC range is set to $\mathrm{SOC}_0^{\max} = 1$ and $\mathrm{SOC}_0^{\min} = 0$ for both the SEIKF and EnKF. Such a tuning process for ensemble-based algorithms requires some minimal manual effort.

Compared with the ensemble-based techniques presented above, the tuning procedure of the UKF is much more complex. In order to maintain the conciseness of the present work, the detailed formulation of the UKF is not provided here but the reader is referred to various works such as [16], [23], [34]. The parameters to be tuned include the initial mean state vector $\hat{\mathbf{x}}_0 \in \mathbb{R}^n$, the initial posterior error covariance $\hat{\mathbf{P}}_0 \in \mathbb{R}^{n \times n}$, as well as three scaling parameters κ, α, and β. Due to the complexity of the electrochemical battery model, how to select the parameters to guarantee the optimal estimator performance has not been explicitly discussed in the relevant works, e.g. [16], [23]. In this work, the scaling parameters are set to $\kappa = 0$, $\alpha = 0.001$, and $\beta = 2$, as recommended in [34], and the initial error covariance is set to $\hat{\mathbf{P}}_0 = (\hat{\mathbf{x}}_0 - \mathbf{x}_0)(\hat{\mathbf{x}}_0 - \mathbf{x}_0)^\top$, although in practice the ground truth $\mathbf{x}_0$ is usually unknown.

C. Constraint on Mass Conservation

The UKF-based battery electrochemical state estimator suffers from the issue of slow convergence and even filter divergence, especially when the estimated error of the initial state is large. This phenomenon is the consequence of the loss of mass conservation in the conventional UKF algorithm, and a general remedy is to impose a constraint on the total mass into the algorithm [16], [23]. In the present study, this is achieved by modifying the posterior state estimate $\hat{\mathbf{x}}_k^+ = [\hat{x}_k^{+(1)}, \hat{x}_k^{+(2)}, \cdots, \hat{x}_k^{+(n)}]^\top$ obtained in the update step of the UKF. Specifically, denoting the new posterior state estimate by $\hat{\mathbf{x}}_{\mathrm{new},k}^+ = [\hat{x}_{\mathrm{new},k}^{+(1)}, \hat{x}_{\mathrm{new},k}^{+(2)}, \cdots, \hat{x}_{\mathrm{new},k}^{+(n)}]^\top$, its qth element $\hat{x}_{k,\mathrm{new}}^{+(q)}$ is calculated as

$$\hat{x}_{\mathrm{new},k}^{+(q)} = \begin{cases} \hat{x}_k^{+(q)} \times \frac{n_{s,\mathrm{tot},k}^{\mathrm{Li}}}{\hat{n}_{s,\mathrm{tot},k}^{\mathrm{Li}}}, & \forall q \in \mathcal{S}_s^{\mathrm{pos}} \cup \mathcal{S}_s^{\mathrm{neg}} \\ \hat{x}_k^{+(q)}, & \text{otherwise} \end{cases} \quad (21)$$

where $n_{s,\mathrm{tot},k}^{\mathrm{Li}}$ is the total mass calculated according to (2) with the unmodified posterior estimate $\hat{\mathbf{x}}_k^+$, while $\hat{n}_{s,\mathrm{tot},k}^{\mathrm{Li}}$ represents the estimated total mass that is equal to $n_{s,\mathrm{tot}0}^{\mathrm{Li}}$ at the BOL and is decreased due to capacity fade.

For the SEIKF-based estimators, we find that the constraint on the mass conservation is intrinsically preserved and there is no need to add the modification step such as (21). In other words, the condition (2) is guaranteed for each member of the posterior state ensemble matrix $\hat{\mathbf{X}}_k^+$ in the kth time step,
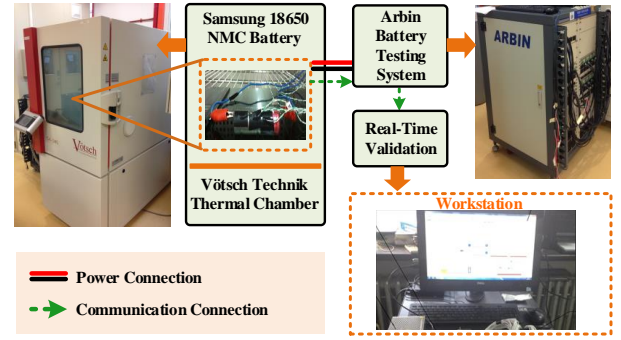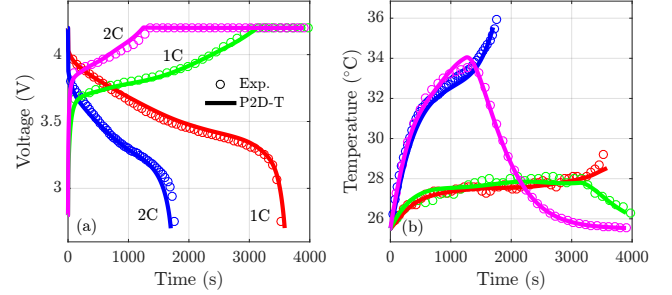

Fig. 3. Experimental setup.

Fig. 4. Comparison of the P2D-T model and experimental measurements under the CC-CV charge and CC discharge protocol: (a) Terminal voltage. (b) Battery temperature.

as long as the member of the previous-step posterior state ensemble matrix $\hat{\mathbf{X}}_{k-1}^+$ satisfies (2). The proof is provided in Appendix B. This advantageous feature of the SEIKF reduces the complexity of the battery estimator design.

V. ILLUSTRATIVE EXAMPLES

In this section, experimental results and numerical study will be provided to validate the proposed electrochemical state estimator for the Li-ion batteries based on the adaptive SEIKF. The full-order P2D-T model was implemented in COMSOL Multiphyiscs 5.3a, and the ROMs and the state estimation algorithms were implemented in MATLAB R2016a environment. All the simulated results were obtained on a 64-bit Windows 10 on a PC with Intel Core 2 Q9400 @ 2.67GHz processor and 8GB RAM with sampling time $\Delta t = 1$ s.

A. Model Validation and Comparison

Experiments were conducted on a 2.6-Ah 18650 high-energy NMC/graphite battery cell to validate the benchmark P2D-T model. The experimental setup shown in Fig. 3 comprises an Arbin battery tester with current/voltage measurements, a thermal chamber for ambient temperature regulation, and a workstation for user-machine interface and data acquisition. The range of the current and voltage sensors inside the test bench are 10 A and 5 V, while the measurement error limits for voltage and current are both within 0.05%. The acquired high-accuracy experimental data including the load current and terminal voltage are collected at 1 Hz. The cell was cycled with constant-current constant-voltage (CC-CV) charge and CC discharge protocol with different current
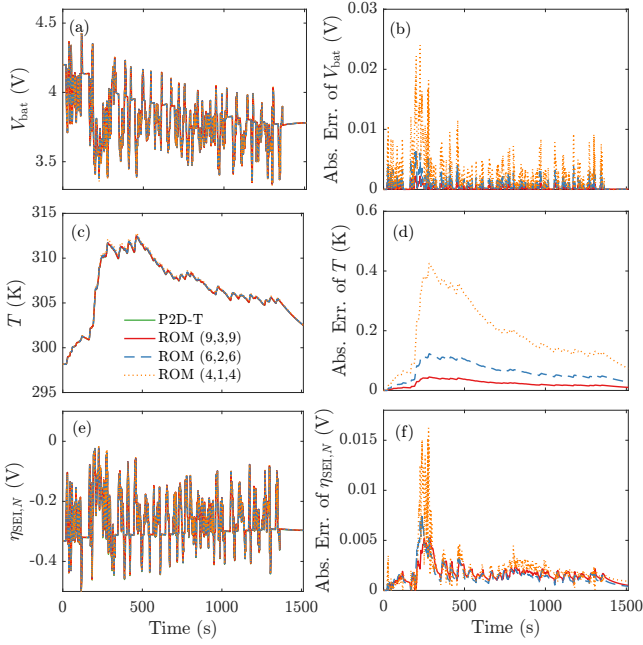
Fig. 5. Comparison of the P2D-T model and the ROM of Li-ion batteries under a testing dynamic driving cycle: (a) Terminal voltage, (b) voltage error, (c) battery temperature, (d) temperature error, (e) SEI potential at the sep/neg boundary, and (f) SEI potential error.
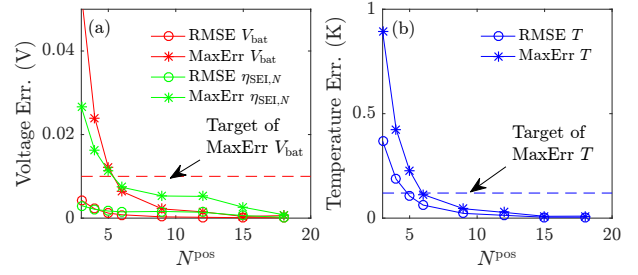

Fig. 6. Accuracy of the ROM with different control volumes. (a) Errors of terminal voltage and SRP at the sep/neg boundary. (b) Errors of battery temperature.

TABLE I
ELECTROCHEMICAL PARAMETERS OF LI-ION BATTERY MODEL

Symbol	pos	sep	neg
R_p [a]	5×10^{-6}	–	5×10^{-6}
L [a]	55.8×10^{-6}	25×10^{-6}	88.0×10^{-6}
ε_e [a]	0.45	–	0.5
ε_s [a]	0.55	–	0.5
c_{e0} [a]		1200	
t_a^0 [a]		0.637	
D_s [b]	1.1×10^{-14}	–	9.96×10^{-15}
$c_{s,\max}$ [b]	$78,552$	–	$35,900$
k_0 [b]	8.7×10^{-12}	–	1.1×10^{-11}
$c_{s,0\%}$ [b]	$74,836$	–	319
$c_{s,100\%}$ [b]	$35,348$	–	$27,859$
C_T [b]		30.1	
R_T [b]		10.0	

OCP of positive electrode (NMC) [c] :

$$U_{\mathrm{ss},i} = f^i_{\mathrm{OCP}}(\theta := c_{\mathrm{ss},i}/c^{\mathrm{pos}}_{s,\max}) = 3.844 \exp(-(\tfrac{\theta - 0.3419}{0.2176})^2)$$
$$+ 2.845 \exp(-(\tfrac{\theta - 0.6332}{0.2026})^2) + 2.643 \exp(-(\tfrac{\theta - 0.8753}{0.1786})^2)$$
$$+ 0.9075 \exp(-(\tfrac{\theta - 0.9683}{0.06277})^2) + 0.3364 \exp(-(\tfrac{\theta - 0.9016}{0.0721})^2)$$

OCP of negative electrode (Graphite) [d] :

$$U_{\mathrm{ss},i} = f^i_{\mathrm{OCP}}(\theta := c_{\mathrm{ss},i}/c^{\mathrm{neg}}_{s,\max}) =$$
$$0.1397 + 0.6892 \exp(-49.2036\theta) + 0.4190 \exp(-254.4\theta) -$$
$$\exp(49.979\theta - 43.379) - 0.02822 \tan^{-1}(22.523\theta - 3.6533) -$$
$$0.01308 \tan^{-1}(28.348\theta - 13.4396)$$

[a] From [36]. [b] Identified using GA. [c] Fitted. [d] From [35].

rates, between the maximum voltage of 4.2 V and the cut-off voltage of 2.7 V. The maximum current limit is 2C for this high-energy type cell according to the specifications. The ambient temperature of the battery is maintained at 25.5°C, i.e., $T_{\mathrm{amb}} = 298.65$ K.

The electrochemical model parameters used in this study are given in Table I. First, the OCP function for the graphite negative electrode was obtained from [35], and the OCP function of the NMC positive electrode was fitted as the sum of measured open-circuit voltage and the OCP of the negative electrode. Sensitivity analysis was next conducted based on voltage and temperature measurements. Most of the material-dependent parameters and/or the parameters with low sensitivities to input variation were obtained from the literature [36], and the remaining parameters were identified using the genetic algorithm (GA) as described in [37]. The measured cell voltage and temperature are compared in Fig. 4 with the simulation results using the P2D-T model. Clearly, the P2D-T model reproduces the battery dynamics with high fidelity over a wide operating range. As the suitability of the P2D-T model for accurately representing the characteristics of Li-ion cells with different types of chemistries has been extensively demonstrated in the literature, the repetitive experimental validation process is not presented.

Since it is difficult to measure the internal variables such as the concentrations and reaction overpotentials in real-time, we follow the common practice in the literature, e.g. [12], [22], [23], by using the above experimentally-verified model as a benchmark to further compare the ROM of the Li-ion battery presented in Section II-B. A modified Federal Urban Driving Schedule (FUDS) test profile was chosen as the input current. The original maximum current rate is 1C and the magnitude

of the profile is amplified by a factor of 8. Different control volume numbers, denoted by the triple $(N^{\mathrm{pos}}, N^{\mathrm{sep}}, N^{\mathrm{neg}})$, are used to evaluate the accuracy and the computation speed of the ROMs, so that a set of suitable control volume numbers can be selected for the state estimator. For simplicity, we select $N^{\mathrm{neg}} = N^{\mathrm{pos}}$ and $N^{\mathrm{sep}} \approx (1/3)N^{\mathrm{pos}}$. The order of solid-phase diffusion model is selected as $M = 2$. The simulated terminal voltage V_{bat}, battery temperature T, and the SEI-related SRP at the sep/neg boundary (denoted by $\eta_{\mathrm{SEI},N}$), as well as their absolute errors to the P2D-T model, are shown in Fig. 5. The root-mean-square errors (RMSEs) and the maximum absolute errors (MaxErrs) are plotted against the number of control volume of the positive electrode N^{pos} in Fig. 6.

Unsurprisingly, the model accuracy increases as the number of control volumes increases in both terms of RMSEs and MaxErrs. The selection of the number of control volumes depends on the requirement of model accuracy for specific
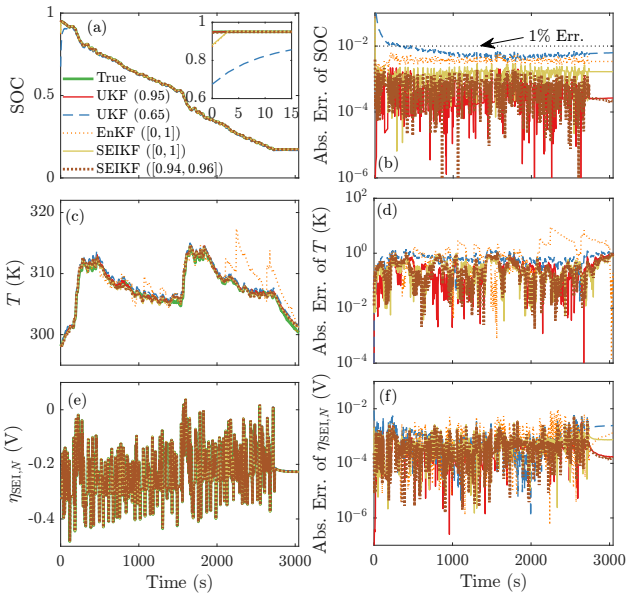
Fig. 7. Comparison of the state estimation results using SEIKF, EnKF, and UKF: (a) SOC, (b) estimation error of SOC, (c) battery temperature, (d) estimation error of battery temperature, (e) SEI potential, and (f) estimation error of SEI potential. Initial SOC or $[\text{SOC}_0^{\min}, \text{SOC}_0^{\max}]$ of the estimator is indicated in the legend.

Fig. 8. Effect of the constraint on mass conservation: (a) SOC, (b) amount of cyclable lithium and SOH.

applications and the affordable computational overheads. In this work, we consider that the model shall be sufficiently accurate if the MaxErrs of the simulated terminal voltage and battery temperature are lower than the standard deviations (SDs) of corresponding measurement errors. Suppose the SDs of the voltage sensor and the temperature sensor are $\sigma_V = 10$ mV and $\sigma_T = 0.1$ K, respectively, by observing Fig. 6, we find that $N^{\text{pos}} = N^{\text{neg}} = 6$ is suitable to be used for designing the electrochemical-thermal model-based state estimators, with the system order being $n = 40$. The improvement in model accuracy by further increasing of the number of control volumes does not bring benefits in practice due to the presence of measurement errors.

B. Comparison of UKF, EnKF, and SEIKF

In this subsection, the performance of the proposed SEIKF-based battery electrochemical state estimator is compared with the nonlinear state estimation algorithms including the EnKF and the UKF. In this case, as a benchmark, a degradation model proposed in [26] with accelerated aging behaviors is used to represent the capacity fade phenomenon as described in (4) and (5), but it is not considered in the design of the state estimator (i.e., k_{deg} in (6) is set to zero). The modified FUDS profile used in Section V-A with the maximum 8C current was repeated twice for the comparison. Based on the testing procedure described in Section IV-B, it is found that $m = 3$ is the minimum ensemble size for the SEIKF to avoid numerical instability in the present investigation based on the selected current profile, and the same m is selected for the EnKF to compare the accuracy of the estimation algorithms. The reference battery external measurements and internal variables are obtained using the benchmark P2D-T model implemented
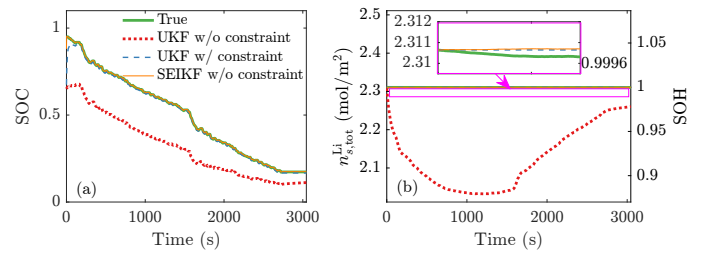
in COMSOL, with the initial SOC being $\text{SOC}_0 = 0.95$. Two SOC values were used for initializing the UKF: One was initialized with the true SOC ($\widehat{\text{SOC}}_0 = \text{SOC}_0 = 0.95$), and the results are considered the optimal benchmark for the evaluation of the accuracy of the estimation. For the other case, the state vector mean $\hat{\mathbf{x}}_0$ of the UKF was initialized with a deviation of 30% on the true SOC, i.e., $\widehat{\text{SOC}}_0 = 0.65$, so that the convergence of the algorithms can be evaluated. In this case, the error covariance matrices are assumed known and constant: $\hat{\mathbf{R}}_k = \mathbf{R}_1 = \text{diag}([\sigma_V^2, \sigma_T^2]) = \text{diag}([0.01^2, 0.1^2])$ and they correspond to the voltage and temperature sensors described in Section V-A. $\hat{\mathbf{Q}}_k = \mathbf{Q}_1$ is a diagonal matrix and each element equals 1×10^{-4}. SOC, battery temperature, SEI potential at sep/pos boundary, and corresponding errors compared to the P2D-T model are shown in Fig. 7 and the performance is summarized in Table II.

TABLE II
COMPARISON OF UKF-, ENKF-, AND SEIKF-BASED BATTERY
ELECTROCHEMICAL STATE ESTIMATORS

	UKF		EnKF		SEIKF
$\widehat{\text{SOC}}_0$	0.95	0.65	–	–	–
$[\text{SOC}_0^{\min}, \text{SOC}_0^{\max}]$	–	–	[0,1]	[0,1]	[0.94, 0.96]
RMSE of SOC (%)	< 0.1	0.6	0.4	0.2	< 0.1
RMSE of T (K)	0.4	0.8	1.8	0.4	0.4
MaxErr of T (K)	1.5	1.8	8.7	1.7	1.5
RMSE of $\eta_{\text{SEI},N}$ (mV)	1.2	2.3	2.4	1.6	1.3
Convergence Time (s)	–	138	3	3	3
CPU Time (s)	66.2	66.2	6.1	6.7	6.7

First, it can be observed that the convergence time of the UKF-based estimator is long if the initial estimate error is large, whereas both the ensemble-based estimators, including the EnKF and the SEIKF, converge rapidly within only a few seconds, thanks to the robust ensemble initialization process presented in Section III-A. The computational burden of the UKF-based estimator is heavy: The CPU time of the UKF is about $9 - 10$ times longer than the ensemble-based methods. This is mainly because a large-size matrix with the dimension $n \times (2n+1) = (40 \times 81)$ has to be processed for the unscented transform in the UKF [34].

Compared to the EnKF, the SEIKF provides a considerable improvement in estimation accuracy. This can be seen from the estimation errors of SOC, temperature, and SEI potential as shown in Figs. 7(b), (d), and (f), respectively. These variables are important for designing safety- and health-aware battery management strategies. Furthermore, as can be seen
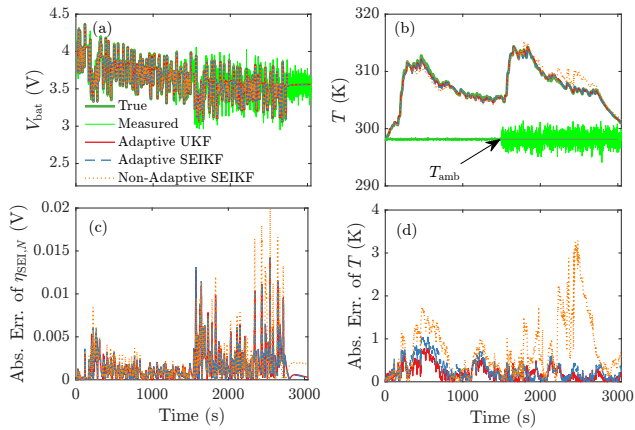
Fig. 9. Comparison of the state estimation results using the non-adaptive SEIKF and the adaptive SEIKF: (a) Voltage, (b) battery and ambient temperatures, (c) estimation error of SRP, and (d) estimation error of battery temperature.

from Fig. 7(c), the EnKF produces an unacceptable erroneous estimate of the temperature, and the MaxErr of the temperature estimate is about 8.7 K. In fact, the proposed SEIKF-based estimator has achieved the accuracy close to the UKF with improved capability for fast convergence, more robust to initial error, while the computational requirement is significantly reduced. The high accuracy of the SEIKF-based estimator can also be verified with increased confidence in the initial SOC range. For example, by choosing $SOC_0^{max} = 0.96$ and $SOC_0^{min} = 0.94$, the simulated performance using SEIKF is closer to the UKF initialized with true SOC, as shown in Fig. 7 and Table II.

In addition, as discussed in Section IV-C, the proposed SEIKF-based battery estimator is mass conservative and thus advantageous over the UKF-based battery state estimator where the step (21) is needed. To demonstrate the benefit, SOC, amount of cyclable lithium, and SOH of the cell are calculated according to (1)–(3) and compared in Fig. 8. It can be seen that the unconstrained UKF-based estimator does not converge to the true states, and the incorporation of the constraint on mass conservation can indeed speed up the process. It can be seen from Fig. 8(b) that during this short period of time, although the side reactions lead to capacity fade and SOH reduction, the influence on battery characteristics is insignificant and the performance of the proposed SEIKF-based battery state estimator has not been affected.

C. Comparison of Adaptive SEIKF, Non-Adaptive SEIKF, and Adaptive UKF

In this subsection, the performance of the adaptive SEIKF-based battery state estimator is evaluated by comparing it with a non-adaptive SEIKF and an adaptive UKF. In this case, the same degradation model as used in Section V-B is adopted to describe the battery capacity fade behavior as explained in Section II-C. In contrast to the previous case, in the design of the state estimator, the degradation coefficient k_{deg} in (6) is monitored and updated to track the slow degradation dynamics. The forgetting factor was tuned using the trial-and-error method and selected as $\delta_R = 0.005$ for both the adaptive

SEIKF and adaptive UKF, which will be described later. The effects of the adaptiveness of the state estimator is two-fold. First, varying measurement covariance is introduced to signify the uncertainty in measurements due to sensor faults: The SD of the voltage measurement increases from $\sigma_V = 10$ mV to 100 mV, and the SD of the temperature measurement increases from $\sigma_T = 0.1$ K to 1 K, both at $t = 1500$ s. To evaluate the robustness of the estimator, the initial σ_V and σ_T were assumed unknown and set to half of the true values. The performance of the estimators are compared in Fig. 9, and the estimated σ_V^2 and σ_T^2 using the adaptive SEIKF is compared with the ground truth in Figs. 10(a) and (b). It can be seen that with the proposed adaptive SEIKF algorithm, the estimation errors of both the SRP and the battery temperature are effectively reduced compared to the case with the non-adaptive SEIKF. With the adaptive scheme, the RMSEs of SRP and temperature estimations have been reduced by 42% from 4.3 mV to 2.5 mV, and by 85% from 1.3 K to 0.2 K, respectively. The MaxErr of battery temperature estimation is limited around 1.0 K, whereas the non-adaptive scheme leads to a MaxErr of 3.3 K. The accuracy of the adaptive SEIKF is observed to be close to the adaptive UKF with much reduced computational load: By introducing the adjustment procedures of the covariance to the SEIKF, the CPU execution time increases slightly from 6.7 s to 7.5 s, and the corresponding CPU time for the adaptive UKF is 81.2 s.

Second, the model error due to battery degradation is effectively monitored but not considered negligible. Although in Section V-B, it is shown that treating the SOH as constant in the short term has ignorable effects on the estimate accuracy of fast dynamics, these small changes on battery degradation will accumulate over the long term. Since the augmented state k_{deg} is a positive parameter and dynamically estimated, as shown in Fig. 10(c), the slow reduction behavior in the SOH was well-captured by the proposed adaptive SEIKF based state estimator. In contrast, the non-adaptive SEIKF is affected by the faulty signal of the sensors, which causes incorrect estimate on battery aging. For the adaptive UKF, since the constraint (21) has to be imposed, the degradation behavior cannot be properly captured but remains at as constant.

Note that the forgetting factor δ_R determines the accuracy of the results and it should be properly selected. The effects of different δ_R on the performance of the adaptive SEIKF-based battery state estimator are shown in Fig. 11. It can be seen from Fig. 11(a) that a small δ_R (e.g., 0.001) will lead to a slow response to the changes in the measurement errors, while Fig. 11(b) shows that a large δ_R (e.g., 0.02) can cause difficulty in correctly tracking the degradation behaviors. The relationships between the δ_R and RMSEs in Fig. 11(e) indicate that although adopting $\delta_R = 0.01$ can achieve the minimum RMSEs for SOC and T, the corresponding SOH estimation error is much larger than $\delta_R = 0.005$. By selecting $\delta_R = 0.005$, the performance is optimal in terms of SOH estimation, and at the same time, acceptable estimation accuracy of SOC and T can be obtained.
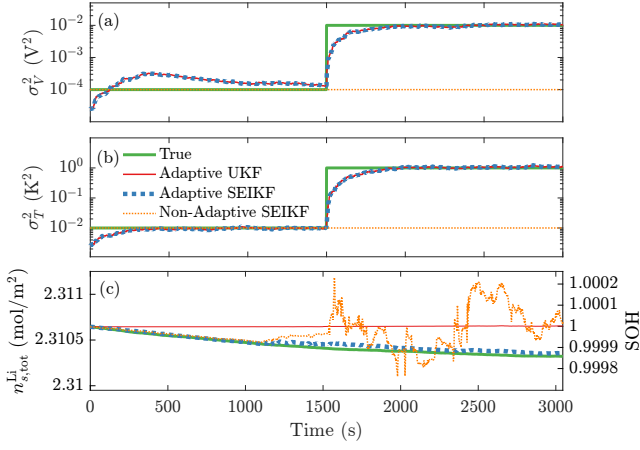
Fig. 10. Estimated measurements error covariance and model error due to aging. (a) Variance of voltage measurement. (b) Variance of temperature measurement. (c) Amount of cyclable lithium.
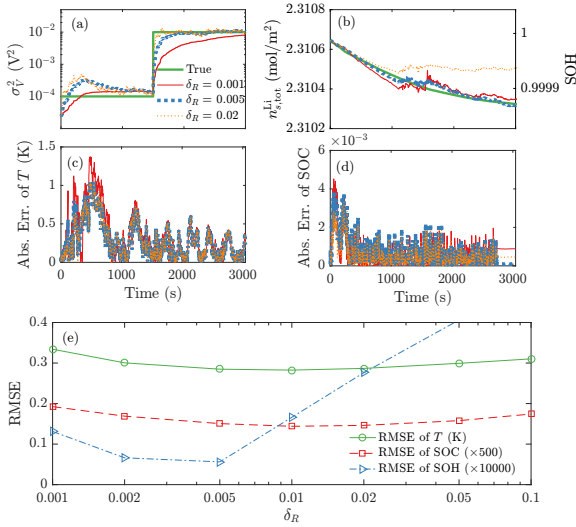

Fig. 11. Effect of varying δ_R on the estimated (a) voltage error variance, (b) amount of cyclable lithium and SOH, (c) temperature error, (d) SOC error, (e) RMSEs.

VI. CONCLUSIONS

An ensemble-based state estimator using the singular evolutive interpolated Kalman filter (SEIKF) is designed to monitor the internal states of a lithium-ion cell considering the distributed-parameter nature of the electrochemical devices. A partial differential-algebraic equation based electrochemical-thermal model is discretized spatially using the finite volume method along the electrode width directions. The resulting high-order system model can be used to precisely predict the internal behaviors of the lithium-ion battery cell regardless of the operating conditions even though it is computationally unaffordable with the existing nonlinear state estimation algorithms. With the intrinsic mass conservation and simple parameter tuning procedure, the proposed SEIKF-based battery state estimator is shown to be superior in estimating the internal distributed states compared to the well-established UKF in terms of computational complexity, and advantageous over the EnKF in terms of accuracy. The uncertainties in the model due

to degradation and measurement errors are properly addressed by adaptively adjusting the covariance matrices.

As one of the Kalman-filter-based nonlinear state estimation techniques, the optimality of the SEIKF relies on the Gaussian assumption for the filtering density function. Hence, further improvement on non-Gaussian conditions should be considered in our future work. Techniques to select the optimal forgetting factors in the proposed adaptive filtering scheme will be investigated. More sophisticated degradation models will also be incorporated for enhanced health-related information monitoring. Such accurate acquisition of the internal battery states provides important health and safety information for the design of some advanced health- and safety-aware charging control strategies.

APPENDIX A
CALCULATION OF MATRIX Ω_k

The matrix Ω_k in (14d) can be determined by the following recursive method with m iterations [28]. Denote ψ the iteration number, thus

1) Iteration $\psi = 1$: Randomly set $\Omega^{(1)} = 1$ or -1, with equal probability.

2) Iterations $\psi = 2, 3, \cdots, m-1$: First, initialize a random vector $\mathbf{a}^{(\psi)} = [a_1, a_2, \cdots, a_\psi]^\top \in \mathbb{R}^\psi$ of unit norm.

Next, calculate the Householder matrix associated with $\mathbf{a}^{(\psi)}$

$$H(\mathbf{a}^{(\psi)}) := \mathbf{I}_{\psi \times \psi} - \frac{1}{|a_\psi| + 1} \underline{\mathbf{a}}^{(\psi)} \underline{\mathbf{a}}^{(\psi)\top} \quad (A.1)$$

where $\underline{\mathbf{a}}^{(\psi)} = [a_1, a_2, \cdots, a_{\psi-1}, a_\psi + \text{sign}(a_\psi)]^\top$.

Then use the first $\psi - 1$ columns of the Householder matrix $H(\mathbf{a}^{(\psi)})$, denoted by $H^*(\mathbf{a}^{(\psi)})$, to compute $\Omega^{(\psi)} \in \mathbb{R}^{\psi \times \psi}$ as

$$\Omega^{(\psi)} = [H^*(\mathbf{a}^{(\psi)})\Omega^{(\psi-1)}, \mathbf{a}^{(\psi)}] \quad (A.2)$$

3) Iteration $\psi = m$: With $\mathbf{a}^{(m)} = (m^{-1/2})\mathbf{1}_{m \times 1}$, the final Ω_k is obtained via

$$\Omega_k = \Omega^{(m)} = H^*(\mathbf{a}^{(\psi)})\Omega^{(m-1)}. \quad (A.3)$$

APPENDIX B
PROOF OF MASS CONSERVATION IN THE SEIKF

For the convenience of notation, the mass conservation condition (2) can be expressed by

$$\mathbf{k}^\top \mathbf{x}_k = n^{\text{Li}}_{s,\text{tot},k} \quad (B.1)$$

where $\mathbf{k} \in \mathbb{R}^n$ is a coefficient vector. It can be readily shown that, if each member of an ensemble $\mathbf{X}_k$ follows (2), the ensemble mean $\bar{\mathbf{x}}_k$ and ensemble perturbation matrix $\tilde{\mathbf{X}}_k$ must satisfy the following conditions:

$$\mathbf{k}^\top \bar{\mathbf{x}}_k = n^{\text{Li}}_{s,\text{tot},k} \quad (B.2)$$

$$\mathbf{k}^\top \tilde{\mathbf{X}}_k = \mathbf{0}_{1 \times n} \quad (B.3)$$

Assume each member of the posterior state ensemble $\hat{\mathbf{X}}^+_{k-1}$ in the $(k-1)$th time step is mass conservative, i.e.,

$$\mathbf{k}^\top \mathbf{x}^{+(p)}_{k-1} = n^{\text{Li}}_{s,\text{tot},k} \quad \forall p \in \{1, 2, \cdots, m\} \quad (B.4)$$

Since the battery model is mass conservative, by forwarding the model according to (11) and ignoring the model error, each

member of the prior state ensemble is also mass conservative. This gives

$$\mathbf{k}^\top \mathbf{x}_k^{-(p)} = \mathbf{k}^\top \bar{\mathbf{x}}_k^- = n_{s,\text{tot},k}^{\text{Li}} \quad \forall p \in \{1, 2, \cdots, m\} \quad \text{(B.5)}$$

$$\mathbf{k}^\top \tilde{\mathbf{X}}_k^- = \mathbf{0}_{1 \times n} \quad \text{(B.6)}$$

Left multiplying (14a) and (14b) by $\mathbf{k}^\top$, and considering (B.5) and (B.6) yields

$$\mathbf{k}^\top \bar{\mathbf{x}}_k^+ = \mathbf{k}^\top \bar{\mathbf{x}}_k^- + \mathbf{k}^\top \tilde{\mathbf{X}}_k^- \bar{\mathbf{w}}_k = \mathbf{k}^\top \bar{\mathbf{x}}_k^- = n_{s,\text{tot},k}^{\text{Li}} \quad \text{(B.7)}$$

$$\mathbf{k}^\top \tilde{\mathbf{X}}_k^+ = \mathbf{k}^\top \tilde{\mathbf{X}}_k^- \tilde{\mathbf{W}}_k = \mathbf{0}_{1 \times n} \quad \text{(B.8)}$$

This proves that each member of the posterior state ensemble $\hat{\mathbf{X}}_k^+$ in the kth time step is also mass conservative.

REFERENCES

[1] Y. Li, M. Vilathgamuwa, S. S. Choi, T. W. Farrell, N. T. Tran, and J. Teague, "Development of a degradation-conscious physics-based lithium-ion battery model for use in power system planning studies," *Appl. Energy*, vol. 248, pp. 512–525, Aug. 2019.

[2] N. A. Chaturvedi, R. Klein, J. Christensen, J. Ahmed, and A. Kojic, "Algorithms for advanced battery-management systems," *IEEE Control Syst. Mag.*, vol. 30, no. 3, pp. 49–68, Jun. 2010.

[3] Y. Gao, X. Zhang, B. Guo, C. Zhu, J. Wiedemann, L. Wang, and J. Cao, "Health-aware multiobjective optimal charging strategy with coupled electrochemical-thermal-aging model for lithium-ion battery," *IEEE Trans. Ind. Informat.*, vol. 16, no. 5, May 2020.

[4] L. De Pascali, F. Biral, and S. Onori, "Aging-aware optimal energy management control for a parallel hybrid vehicle based on electrochemical-degradation dynamics," *IEEE Trans. Veh. Technol.*, vol. 69, no. 10, pp. 10 868–10 878, Oct. 2020.

[5] J. Meng, D. Stroe, M. Ricco, G. Luo, and R. Teodorescu, "A simplified model-based state-of-charge estimation approach for lithium-ion battery with dynamic linear model," *IEEE Trans. Ind. Electron.*, vol. 66, no. 10, pp. 7717–7727, Oct. 2019.

[6] K. Liu, Y. Shang, Q. Ouyang, and W. D. Widanage, "A data-driven approach with uncertainty quantification for predicting future capacities and remaining useful life of lithium-ion battery," *IEEE Trans. Ind. Electron.*, vol. 68, no. 4, pp. 3170–3180, Apr. 2021.

[7] M. Doyle and J. Newman, "Modeling the performance of rechargeable lithium-based cells: design correlations for limiting cases," *J. Power Sources*, vol. 54, no. 1, pp. 46–51, Mar. 1995.

[8] D. Di Domenico, A. Stefanopoulou, and G. Fiengo, "Lithium-ion battery state of charge and critical surface charge estimation using an electrochemical model-based extended Kalman filter," *J. Dyn. Syst. Meas. Control*, vol. 132, no. 6, p. 061302, Nov. 2010.

[9] N. T. Tran, D. M. Vilathgamuwa, Y. Li, T. W. Farrell, S. S. Choi, and J. Teague, "State of charge estimation of lithium ion batteries using an extended single particle model and sigma-point Kalman filter," in *Proc. IEEE Southern Power Electron. Conf.*, Puerto Varas, Chile, 4-7 Dec. 2017, pp. 624–629.

[10] S. J. Moura, F. B. Argomedo, R. Klein, A. Mirtabatabaei, and M. Krstic, "Battery state estimation for a single particle model with electrolyte dynamics," *IEEE Trans. Control Syst. Technol.*, vol. 25, no. 2, pp. 453–468, Mar. 2017.

[11] X. Hu, D. Cao, and B. Egardt, "Condition monitoring in advanced battery management systems: Moving horizon estimation using a reduced electrochemical model," *IEEE/ASME Trans. Mechatronics*, vol. 23, no. 1, pp. 167–178, Feb. 2018.

[12] C. Zou, X. Hu, Z. Wei, T. Wik, and B. Egardt, "Electrochemical estimation and control for lithium-ion battery health-aware fast charging," *IEEE Trans. Ind. Electron.*, vol. 65, no. 8, pp. 6635–6645, Aug. 2018.

[13] B. Liu, X. Tang, and F. Gao, "Joint estimation of battery state-of-charge and state-of-health based on a simplified pseudo-two-dimensional model," *Electrochim. Acta*, vol. 344, p. 136098, Jun. 2020.

[14] X.-G. Yang and C.-Y. Wang, "Understanding the trilemma of fast charging, energy density and cycle life of lithium-ion batteries," *J. Power Sources*, vol. 402, pp. 489–498, Oct. 2018.

[15] J. Sturm, H. Ennifar, S. V. Erhard, A. Rheinfeld, S. Kosch, and A. Jossen, "State estimation of lithium-ion cells using a physicochemical model based extended Kalman filter," *Appl. Energy*, vol. 223, pp. 103–123, Aug. 2018.

[16] S. Marelli and M. Corno, "Model-based estimation of lithium concentrations and temperature in batteries using soft-constrained dual unscented Kalman filtering," *IEEE Trans. Control Syst. Technol.*, vol. 29, no. 2, pp. 926–933, Mar. 2021.

[17] A. Tulsyan, Y. Tsai, R. B. Gopaluni, and R. D. Braatz, "State-of-charge estimation in lithium-ion batteries: A particle filter approach," *J. Power Sources*, vol. 331, pp. 208–223, Nov. 2016.

[18] H. Fang, N. Tian, Y. Wang, M. Zhou, and M. A. Haile, "Nonlinear Bayesian estimation: From Kalman filtering to a broader horizon," vol. 5, no. 2, pp. 401–417, Mar. 2018.

[19] Y. Li, B. Xiong, D. M. Vilathgamuwa, Z. Wei, C. Xie, and C. Zou, "Constrained ensemble Kalman filter for distributed electrochemical state estimation of lithium-ion batteries," *IEEE Trans. Ind. Informat.*, vol. 17, no. 1, pp. 240–250, Jan. 2021.

[20] G. Evensen, "The ensemble Kalman filter for combined state and parameter estimation," *IEEE Control Syst. Mag.*, vol. 29, no. 3, pp. 83–104, Jun. 2009.

[21] G. Burgers, P. J. van Leeuwen, and G. Evensen, "Analysis scheme in the ensemble Kalman filter," *Mon. Weather Rev.*, vol. 126, no. 6, pp. 1719–1724, Jun. 1998.

[22] Y. Bi and S.-Y. Choe, "An adaptive sigma-point Kalman filter with state equality constraints for online state-of-charge estimation of a Li(NiMnCo)O$_2$/carbon battery using a reduced-order electrochemical model," *Appl. Energy*, vol. 258, p. 113925, Jan. 2020.

[23] W. Li, Y. Fan, F. Ringbeck, D. Jöst, X. Han, M. Ouyang, and D. U. Sauer, "Electrochemical model-based state estimation for lithium-ion batteries with adaptive unscented Kalman filter," *J. Power Sources*, vol. 476, p. 228534, Nov. 2020.

[24] Y. Li, M. Vilathgamuwa, T. Farrell, S. S. Choi, N. T. Tran, and J. Teague, "A physics-based distributed-parameter equivalent circuit model for lithium-ion batteries," *Electrochim. Acta*, vol. 299, pp. 451–469, Mar.

[25] C. R. Birkl, M. R. Roberts, E. McTurk, P. G. Bruce, and D. A. Howey, "Degradation diagnostics for lithium ion cells," *J. Power Sources*, vol. 341, pp. 1–35, Feb. 2016.

[26] P. Ramadass, B. Haran, P. M. Gomadam, R. White, and B. N. Popov, "Development of first principles capacity fade model for Li-ion cells," *J. Electrochem. Soc.*, vol. 151, no. 2, pp. A196–A203, Jan. 2004.

[27] X. Jin, A. Vora, V. Hoshing, T. Saha, G. Shaver, R. E. García, O. Wasynczuk, and S. Varigonda, "Physically-based reduced-order capacity loss model for graphite anodes in Li-ion battery cells," *J. Power Sources*, vol. 342, pp. 750–761, Feb. 2017.

[28] D. T. Pham, "A singular evolutive interpolated Kalman filter for data assimilation in oceanography," Laboratoire de Modélisation et Calcul, Grenoble, France, Tech. Rep. RT 163, Sep. 1996.

[29] D. T. Pham, "Stochastic methods for sequential data assimilation in strongly nonlinear systems," *Mon. Weather Rev.*, vol. 129, no. 5, pp. 1194–1207, May 2001.

[30] L. Nerger, T. Janjić, J. Schröter, and W. Hiller, "A unification of ensemble square root Kalman filters," *Mon. Weather Rev.*, vol. 140, no. 7, pp. 2335–2345, Jul. 2012.

[31] S. Akhlaghi, N. Zhou, and Z. Huang, "Adaptive adjustment of noise covariance in Kalman filter for dynamic state estimation," in *Proc. IEEE Power Energy Soc. General Meeting*, Chicago, IL, USA, 16-20 Jul. 2017, pp. 1–5.

[32] J. Zhou, S. Knedlik, and O. Loffeld, "INS/GPS tightly-coupled integration using adaptive unscented particle filter," *J. Navig.*, vol. 63, no. 3, pp. 491–511, May 2010.

[33] L. Nerger, W. Hiller, and J. Schröter, "A comparison of error subspace Kalman filters," *Tellus A: Dyn. Meteorol. Oceanogr.*, vol. 57, no. 5, pp. 715–735, Jan. 2005.

[34] E. A. Wan and R. van der Merwe, "The unscented Kalman filter for nonlinear estimation," in *Proc. IEEE Adaptive Syst. Signal Process., Commun. Control Symp.*, Lake Louise, AB, Canada, 1-4 Dec. 2000, pp. 153–158.

[35] M. Guo, G. Sikha, and R. E. White, "Single-particle model for a lithium-ion cell: Thermal behavior," *J. Electrochem. Soc.*, vol. 158, no. 2, pp. A122–A132, 2011.

[36] X. Kang, W. Shi, and H. Chen, "Parameter identification based on simplified electrochemical model of lithium ion battery," *Energy Storage Sci. Technol.*, vol. 9, no. 3, pp. 969–978, May 2020.

[37] J. Li, L. Zou, F. Tian, X. Dong, Z. Zou, and H. Yang, "Parameter identification of lithium-ion batteries model to predict discharge behaviors using heuristic algorithm," *J. Electrochem. Soc.*, vol. 163, no. 8, pp. A1646–A1652, Jun. 2016.